CHEMISTRY OF MATERIALS

Article

pubs.acs.org/cm

Structure and Electrochemistry of Two-Electron Redox Couples in Lithium Metal Fluorophosphates Based on the Tavorite Structure

Brian L. Ellis,[†] T. N. Ramesh,[†] Linda J.M. Davis,[‡] Gillian R. Goward,[‡] and Linda F. Nazar*[,†]

[†]Department of Chemistry, University of Waterloo, Waterloo, Ontario, Canada N2L 3G1

[‡]Department of Chemistry, McMaster University, Hamilton, Ontario, Canada L8S 4L8

ABSTRACT: An electrochemical and structural study of the two-electron redox couple comprising the tavorite-type series of fluorophosphates $Li_{1\pm x}VPO_4F$ (x = 0, 1) shows that both intercalation of $LiVPO_4F$ with Li (to give Li_2VPO_4F) and deintercalation (to give VPO_4F) proceed by a two-phase mechanism. Structural models for each of the three phases were determined by Rietveld refinements of combined neutron and X-ray diffraction data of the isolated pure phase materials. $LiVPO_4F$ crystallizes in the triclinic space group $P\bar{1}$ and is isostructural to many known fluorophosphates whereas both Li_2VPO_4F and VPO_4F crystallize in the monoclinic space group $C2/c$, although they have very closely related structures to the parent. Solid-state ^{6,7}Li NMR studies of Li_2VPO_4F reveal the two lithium sites are clearly distinguishable, with more than 100 ppm separation between the resonances. 2D exchange NMR is used to demonstrate the time scale of ion dynamics between the two sites.

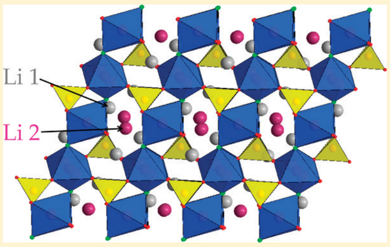

KEYWORDS: *Li-ion battery, Li-ion two-electron redox couple, lithium metal fluorophosphate, tavorite, cathode, solid-state Li NMR, 2D NMR*

INTRODUCTION

Lithium transition metal phosphate and fluorophosphates are important positive electrode materials for safe, low-cost lithium-ion cells. The most prominent compounds of this group studied to date have been the olivine phosphates, namely $LiFePO_4$[1,2] and $LiMnPO_4$.[3,4] Because of structural nuances, the olivine $LiFePO_4$ has a higher voltage (3.5 V) than most other iron phosphates,[5,6] which allows the fabrication of Li-ion cells with high energy densities. The major limitations of $LiFePO_4$, namely poor electrical conductivity[7,8] and one-dimensional Li-ion diffusion,[9] have been partially overcome by decreasing the crystallite size to the nanoscale[10,11] and coating conductive additives onto the surface.[12−14] However, these approaches add to the complexity of the material's manufacture.

This has prompted us to explore the next generation of cathode materials that might exhibit more attractive features with fewer inherent limitations. In the search for structural frameworks that overcome the 1D ion conductivity challenge of olivine, a variety of fluorophosphates have been revealed as attractive compounds. Na_2FePO_4F has been shown to exhibit solid-solution behavior when cycled in a lithium cell and has an average potential of 3.3 V vs Li/Li^+.[15] The compound also exhibits good ionic conductivity as evidenced by the ease of Na^+/Li^+ ion exchange upon both electrochemical cycling and via chemical methods.[16] This compound also benefits from a low volume change on electrochemical cycling.[15]

Another important class of fluorophosphates materials comprises compounds based on the tavorite ($LiFePO_4OH$) structure.[17] There are several known compounds of this structure type including $LiAlPO_4OH$,[18] $LiAlPO_4F$,[18] $LiMnPO_4OH$,[19] $LiGaPO_4OH$,[20] and fluorosulphates such as $LiMgSO_4F$[21] and $LiFeSO_4F$.[22,23] The spacious structure contains Li tunnels in multiple directions which allows for good Li-ion transport in these materials. Up to this point, two fluorophosphates from this family have been explored as potential Li-ion battery cathodes: $LiFePO_4F$[24,25] and $LiVPO_4F$.[26−28] $LiFePO_4F$ is a promising positive electrode material with a potential of 2.8 V and its synthesis by solid-state and ionothermal methods have been reported previously.[24,25] $LiVPO_4F$ was first reported in 2003 as a 4.1 V positive electrode material with a theoretical capacity of 155 mA h/g, corresponding to the extraction of one Li.[26] Interestingly, it was later shown that $LiVPO_4F$ could also intercalate Li at a potential of about 1.8 V.[29] Since $LiVPO_4F$ was shown to function as both a positive and negative electrode, this led to the report of a $LiVPO_4F/LiVPO_4F$ symmetric cell with one electrode working on the $V^{3+} \rightarrow V^{4+}$ redox couple and the other working on the $V^{3+} \rightarrow V^{2+}$ redox couple.[29]

Although structural data exist on the parent $LiVPO_4F$, no such data exist on the electrode materials upon discharge or charge. Here we report the structure of the reduced tavorite phase Li_2VPO_4F, determined by a combined refinement of X-ray and neutron diffraction, as well as the structure of the fully oxidized VPO_4F. X-ray diffraction and electrochemical studies were used to confirm the mechanism of lithium (de)-intercalation for each compound. ^{6,7}Li solid-state NMR was also used to probe the Li positions and occupancies in both

Received: June 22, 2011
Revised: October 14, 2011
Published: November 3, 2011

$LiVPO_4F$ and the reduced phase Li_2VPO_4F. Our findings reveal the important structural factors that underlie the high degree of reversibility in this two electron electrochemical couple.

EXPERIMENTAL SECTION

Synthetic Methods. *$LiVPO_4F$.* Our synthesis was similar to the method reported by Barker et al.[26] V_2O_5 (Aldrich, 99%+), $NH_4H_2PO_4$ (BDH, 99%) and carbon black were mixed in a 0.5:1:1.5 molar ratio and fired at 750 °C under a flowing Ar atmosphere to produce VPO_4/C. Stoichiometric amounts of VPO_4/C and LiF were ground in zirconia milling media and subsequently fired at 600 °C for 1 h under an Ar atmosphere.

$Li_{1+x}VPO_4F$. $LiVPO_4F$ was stirred with a stoichiometric amount of $LiAlH_4$ in tetrahydrofuran in an argon-filled glovebox for 44 h. The product was washed with tetrahydrofuran and stored under argon.

$Li_{1-x}VPO_4F$. Stoichiometric amounts of $LiVPO_4F$ and $NOBF_4$ were stirred in acetonitrile in an argon-filled glovebox for 16 h. The product was filtered, rinsed with acetonitrile and dried under ambient conditions.

Analytical Methods. Inductively coupled plasma mass spectroscopy (ICP-MS), as per EPA 3050, was also used to determine elemental composition.

Laboratory X-ray Diffraction. X-ray diffraction measurements were performed on a Bruker D8 Advance powder diffractometer using Cu−Kα radiation (λ = 1.5405 Å) from 2θ = 10 to 80 degrees, at a count rate of 10 s per step of 0.02°. X-ray diffraction patterns of $Li_{1+x}VPO_4F$ were collected using a hermetically sealed holder owing to the air-sensitivity of these compounds.

Synchrotron X-ray Diffraction. High resolution synchrotron powder diffraction data on $LiVPO_4F$ (motivated by the low symmetry of the unit cell (P-1) and investigation of the occupancies of the split Li site) were collected using beamline 11-BM at the Advanced Photon Source (APS), at the Argonne National Laboratory using an average wavelength of 0.4122 Å. Discrete detectors covering an angular range from −6 to 16° 2θ are scanned over a 34° 2θ range, with data points collected every 0.001° 2θ and scan speed of 0.01°/s.

The 11-BM instrument uses X-ray optics with two platinum-striped mirrors and a double-crystal Si(111) monochromator, where the second crystal has an adjustable sagittal bend.[30] Ion chambers monitor incident flux. A vertical Huber 480 goniometer, equipped with a Heidenhain encoder, positions an analyzer system comprised of twelve perfect Si(111) analyzers and twelve Oxford-Danfysik $LaCl_3$ scintillators, with a spacing of 2° 2θ.[31] Analyzer orientation can be adjusted individually on two axes. A three-axis translation stage holds the sample mounting and allows it to be spun, typically at ~5400 rpm (90 Hz). A Mitsubishi robotic arm is used to mount and dismount samples on the diffractometer.[32] An Oxford Cryosystems Cryostream Plus device allows sample temperatures to be controlled over the range 80−500 K when the robot is used.

The diffractometer is controlled via EPICS.[33] Data are collected while continually scanning the diffractometer 2θ arm. A mixture of NIST standard reference materials, Si (SRM 640c) and Al_2O_3 (SRM 676) is used to calibrate the instrument, where the Si lattice constant determines the wavelength for each detector. Corrections are applied for detector sensitivity, 2θ offset, small differences in wavelength between detectors, and the source intensity, as noted by the ion chamber before merging the data into a single set of intensities evenly spaced in 2θ.

Neutron Diffraction. The neutron diffraction pattern of Li_2VPO_4F was collected on a sample in a sealed holder under an Ar atmosphere owing to its air-sensitivity, using POLARIS, the time-of-flight (TOF) neutron diffraction instrument at ISIS (Rutherford Appleton Laboratories, Didcot, UK). During the fitting of the diffraction data, two neutron banks (under 90° and 145° with respect to the incident beam) were simultaneously fitted with the X-ray data; each bank was equally weighted. For neutron TOF diffraction the incident wavelength is less well-defined than the X-ray data, thus the simultaneous fit was restricted to the lattice parameters from fitting the X-ray data. This was achieved by allowing the neutron diffractometer constants to vary (effectively the exact sample position in the neutron flight path). To correct for an error in the vertical alignment, a diffractometer constant zero term was fitted. The natural abundance of ^{6}Li necessitated the neutron data be corrected for a wavelength-dependent absorption correction, commonly used for TOF neutron diffraction.

Rietveld Refinement. Refinement of $LiVPO_4F$ and VPO_4F (synchrotron X-ray) and Li_2VPO_4F (combined laboratory X-ray and neutron) were carried out using GSAS software[34] with the EXPGUI interface.[35] Both the neutron and the X-ray diffraction line shape were fitted using function type 3 in GSAS. The cell parameters for VPO_4F and Li_2VPO_4F were first determined by indexing with TOPAS software from Bruker. Subsequent Rietveld refinement analysis was carried out initially using fractional coordinates from $LiFePO_4OH$,[18] or $Li(TaO)GeO_4$.[36] Scale factor, zero point, lattice parameters, atomic positions, and thermal factors were iteratively refined.

Elemental Analysis. Inductively coupled plasma mass spectroscopy (ICP-MS), as per EPA 3050, was also used to determine the relative quantities of Li, V, and P.

Electrochemistry. The $LiVPO_4F$/C composite, carbon (Super S) and poly(vinylidene fluoride), PVDF, were mixed in a 87:3:10 mass ratio. N-methyl pyrollidinone was added to this mixture and the resultant slurry was cast on C-coated Al foil and dried for 24 h under vacuum. Circular discs cut from this foil were cycled in coin cells vs. metallic Li with 1 M $LiPF_6$ in ethylene carbonate and dimethyl carbonate in a 1:1 volume ratio as the electrolyte. The cells underwent galvanic cycling on a Biologic VMP3 instrument at a rate of C/10 (1 Li in 10 h).

Solid-State NMR. ^{7}Li and ^{6}Li MAS NMR experiments were performed at Larmor frequencies of 116.6 and 44.1 MHz, respectively, on a Bruker AV300 spectrometer. A custom built probe supporting 1.8 mm rotors was used with MAS frequencies ranging from 25 to 40 kHz. By adjusting spinning speeds from 25 kHz to 40 kHz, a temperature range of 303 to 330 K was available. Both ^{6}Li and ^{7}Li 1D spectra were acquired using 90° pulse lengths ranging from 2.0 to 2.5 μs and recycle delay of 100 ms. Spin−lattice relaxation times (T_1) were determined using the standard inversion recovery sequence included in the Bruker software package. Two-dimensional exchange (EXSY) spectra were acquired using mixing times ranging from 2 to 17 ms. The number of slices in the indirect dimension was 2048. Phase-sensitive detection in t_1 was achieved through the use of States-TPPI.[37]

^{6}Li{^{19}F} REDOR studies were carried out on a Bruker AV500 spectrometer with ^{6}Li and ^{19}F Larmor frequencies of 73.6 and 469.5 MHz, respectively. The same 1.8 mm probe as described above was used for these experiments with the ^{1}H channel modified to allow for ^{19}F dephasing. A ^{19}F π pulse length of 4.40 μs was used. All spectra were referenced to 1 M ^{6,7}LiCl (aq) (0 ppm), and $CFCl_3$ for ^{19}F experiments. Temperatures were calibrated using $Sm_2Sn_2O_7$ as described elsewhere.[38]

RESULTS AND DISCUSSION

Structure. Carbon-coated $LiVPO_4F$ was successfully prepared by a solid-state route similar to a previous report.[26] A high-resolution X-ray diffraction pattern obtained at a synchrotron source along with its Rietveld refinement is shown in Figure 1 and the results are listed in Table 1. $LiVPO_4F$ adopts the tavorite structure and is isostructural with several known hydroxyphosphates such as $LiFePO_4OH$[17] and fluorophosphates including $LiAlPO_4F$, which crystallize in the triclinic space group $P\bar{1}$. Figure 2 depicts the crystal structure derived from the refinement. [$V^{3+}F_2O_4$] octahedra form corner-sharing chains in the (010) direction, where alternate octahedra are tilted. The F ligands act as the bridging ligands. These chains are connected by corner-sharing phosphate tetrahedra to make a spacious 3D framework: wide tunnels (>3 Å in diameter) are present along all of the (100), (010), and (001)

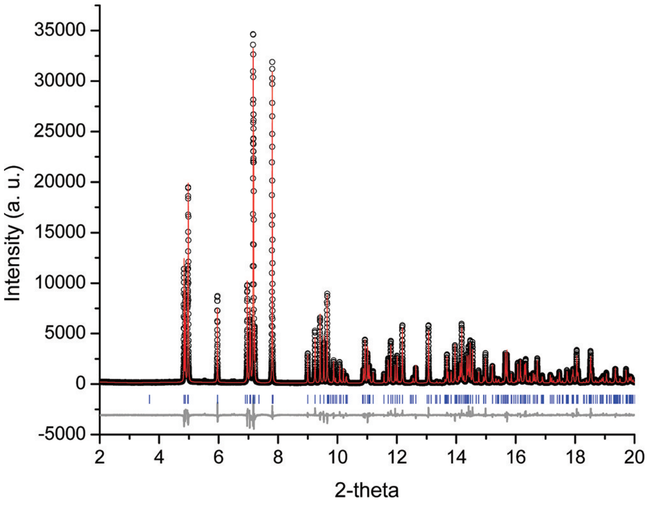

Figure 1. Synchrotron X-ray diffraction pattern ($\lambda = 0.4122$ Å) and Rietveld refinement of $LiVPO_4F$ synthesized by a solid-state method. The experimental points are black, the fit is shown in red, the calculated reflections are shown in blue and the difference map is shown in gray. The lattice parameters and atomic positions are listed in Table 1.

directions. The refined unit cell volume of 174.31 Å^3 is very similar to that reported by Barker and co-workers[26] of 174.35 Å^3, even though the choice of the two triclinic cells differed, as evidenced by the difference in angles between the two reported cells.

It is widely known that lithium fluorophosphates with the tavorite structure favor a low-symmetry octahedral lithium site with a large anisotropic thermal parameter, which is usually refined as a split lithium position, such as in $LiAlPO_4F$. This is also true for $LiVPO_4F$ (see Table 2). Refinements using a single Li site (isotropic thermal parameter) provided much higher R_{wp} values than using a split site to describe the lithium

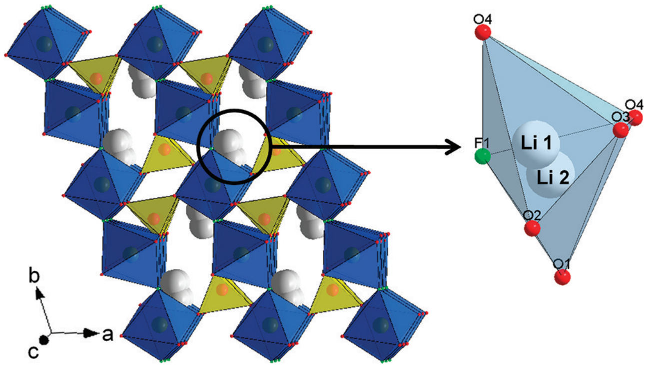

Figure 2. Pictorial representation of the structures of $LiVPO_4F$ with a close-up view of the split lithium position. The vanadium octahedra are shown in blue, phosphate tetrahedra are shown in yellow, and the Li atoms are shown in white.

coordination. The distribution of lithium over these sites varies based on the method of preparation and the nature of the anion (OH vs F) as these factors influence the geometry of the site itself.[39] The lithium co-ordination in $LiVPO_4F$ is shown in Figure 2 and bond distances are summarized in Table 2. In $LiVPO_4F$, the centers of the two Li sites Li1 and Li2 are approximately 0.79 Å apart. The Li1 site has one Li−F bond and two Li−O bonds that are 1.92−2.12 Å in length, all of which are consistent for bond distances with Li in a 4-coordinate environment. Two additional oxygen ligands are 2.29 and 2.43 Å from the Li1 site, thus the Li1 environment may be described as 5-coordinate geometry. The last oxygen ligand is greater than 3 Å from Li1. In contrast, the Li2 site may be described as having [5 + 1] geometry. Li2 has one close F ligand and 4 oxygen ligands at distances varying between 1.98 and 2.32 Å. A fifth oxygen ligand (O3) is 2.88 Å from Li2. With the difference in coordination and bond lengths, it is not surprising that the two Li sites are not equally

Table 1. Lattice Constants and Atomic Parameters of $LiVPO_4F$ Refined from Powder XRD Data[a]

$LiVPO_4F$

space group: $P\bar{1}$ (No. 2), triclinic
$M_w = 171.85$ g/mol
$D = 3.274$ g cm^{-3}
$a = 5.30941(1)$ Å
$b = 7.49936(2)$ Å
$c = 5.16888(1)$ Å
$\alpha = 112.933(0)°$
$\beta = 81.664(0)°$
$\gamma = 113.125(0)°$
$V = 174.306(0)$ Å^3

atom	Wychoff	x/a	y/b	z/c	Occ.	U_{iso}
Li (1)	2*i*	0.389(2)	0.334(1)	0.659(2)	0.18(1)	0.015
Li (2)	2*i*	0.373(2)	0.236(1)	0.517(2)	0.82(1)	0.015
V (1)	1*a*	0	0	0	1.0	0.0043(3)
V (2)	1*b*	0	1/2	1/2	1.0	0.0059(3)
P (1)	2*i*	−0.6476(2)	−0.2515(2)	0.0719(2)	1.0	0.0070(3)
O (1)	2*i*	0.2109(4)	−0.0936(3)	0.1701(4)	1.0	0.015(2)
O (2)	2*i*	−0.3420(4)	−0.1375(3)	0.1705(4)	1.0	0.016(2)
O (3)	2*i*	−0.7627(4)	−0.4100(3)	0.2163(4)	1.0	0.013(2)
O (4)	2*i*	−0.6695(4)	−0.3597(3)	−0.2503(4)	1.0	0.014(2)
F (1)	2*i*	0.0875(3)	0.2450(2)	0.3585(3)	1.0	0.015(2)

[a] Agreement factors: $R_{wp} = 10.30\%$, $R_p = 7.88\%$, $R_F{}^2 = 3.45\%$.

Table 2. Summary of Bond Distances for Li Environment in $LiVPO_4F$ and Li_2VPO_4F

atom	ligand	distance (Å)
	$LiVPO_4F$	
atom	ligand	distance (Å)
Li1	Li2	0.795
	O2	1.919
	O3	1.970
	F1	2.117
	O4′	2.293
	O4	2.428
	O1	3.092
Li2	Li1	0.795
	F1	1.861
	O2	1.983
	O4	2.112
	O3	2.275
	O1	2.323
	O4′	2.881
	Li_2VPO_4F	
atom	ligand	distance (Å)
Li1	F1	2.062
	O2e	2.071
	O2b	2.135
	O1b	2.183
	O1a	2.399
	O1c	2.479
Li2	F1c	1.824
	O2d	1.826
	O1b	1.994
	O2b	2.008
	F1a	2.492
	O1d	2.759

occupied. In our refinement, the occupancy of the Li1 and Li2 sites was found to be 18 and 82% respectively as corroborated by NMR measurements (vide infra). The higher thermodynamic stability that results from the larger number of ligands in the Li2 site renders it the slightly preferred Li environment. This is not the case in $LiFePO_4(OH)$,[17] where the relative occupancy of the Li1 and Li2 sites in that structure is reported to be 1:1.

Electrochemistry. Figure 3 depicts the full electrochemical curve of $LiVPO_4F$, starting with discharge (red arrow). At a rate of C/10, 0.85 Li may be intercalated into the material at a potential of 1.8 V (vs. Li/Li^+). The observed flat plateau of the electrochemical profile in this region implies the reduction of $LiVPO_4F$ to Li_2VPO_4F proceeds via a two-phase process. This is in contrast to the case of reduction of $LiFePO_4F$[24] and $LiFePO_4(OH)$[40] where approximately half of the electrochemical curve exhibited sloping behavior. Charging the cell back to $LiVPO_4F$ shows the same two-phase behavior. As the reoxidation of V^{2+} to V^{3+} nears completion, we observe a rise in the voltage up to 4.25 V which occurs between $Li_{1.25}VPO_4F$ and $LiVPO_4F$, unlike the more gradual voltage rise to 4.25 V between $Li_{1.25}VPO_4F$ and $Li_{0.87}VPO_4F$ observed in Barker's study.[29] The oxidation process continues (from V^{3+} to V^{4+}) on two new plateaus (4.25 V vs Li/Li^+ for $Li_{1-x}VPO_4F$, $0 < x < 0.35$ and 4.3 V vs Li/Li^+ for $Li_{1-x}VPO_4F$, $0.35 < x < 1.0$) until complete oxidation is achieved. Reintercalation of the VPO_4F occurs at 4.20 V vs Li/Li^+ and once 1.0 Li has been intercalated, the potential drops sharply to 1.8 V where intercalation to Li_2VPO_4F continues. The hysteresis must arise from kinetic effects, where insertion of the second lithium is more difficult than its deinsertion owing to volume expansion.

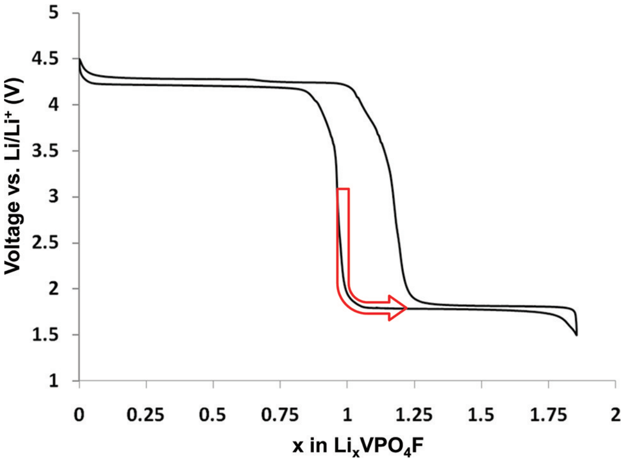

Figure 3. Electrochemical curve of $LiVPO_4F/C$ composite cycled vs Li/Li^+ starting in discharge (as shown by the red arrow). The active material loading was 5 mg/cm^2 and the cell was cycled at a rate of C/10.

We prepared various compositions of $Li_{1-x}VPO_4F$ ($0 \leq x \leq 1$) by chemical oxidation (with $NOBF_4$) and $Li_{1+x}VPO_4F$ ($0 \leq x \leq 1$) by chemical reduction (with $LiAlH_4$) of $LiVPO_4F$ to verify the two-phase nature of each vanadium redox step observed in the electrochemistry. Indeed, X-ray diffraction also shows this to be the case. Figure 4 depicts the evolution of $Li_{1+x}VPO_4F$ from $x = 0$ to $x = 1$ formed upon chemical reduction of $LiVPO_4F$ with $LiAlH_4$ under Ar atmosphere. Due to the instability of V(II) compounds, the diffraction patterns were also collected in a sealed sample holder filled with Ar. Once $LiVPO_4F$ has reduced to $Li_{1.25}VPO_4F$, some of the starting $LiVPO_4F$ material remains and a new phase is present in the diffraction pattern. Additional reduction to $Li_{1.5}VPO_4F$ shows further reduction of the signal intensity of $LiVPO_4F$ and increased intensity of the new reduced phase. Subsequent reduction steps show the same trend: growth of reduced phase at the expense of

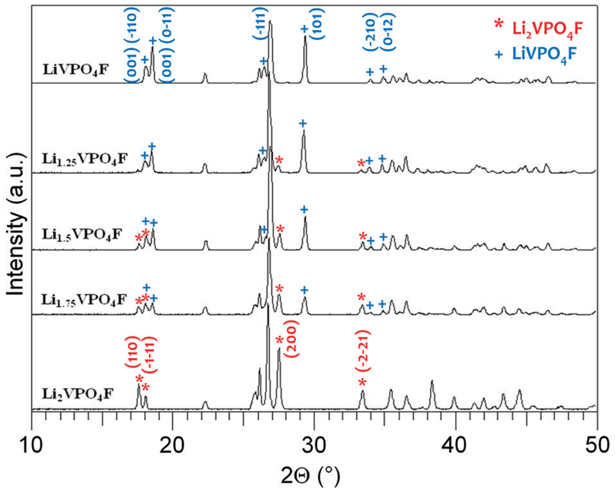

Figure 4. X-ray powder diffraction patterns of $Li_{1+x}VPO_4F$, synthesized by the chemical reduction of $LiVPO_4F$ with $LiAlH_4$. Two-phase behavior was observed as the quantity of $LiVPO_4F$ decreases and the quantity of Li_2VPO_4F increases with increasing x.

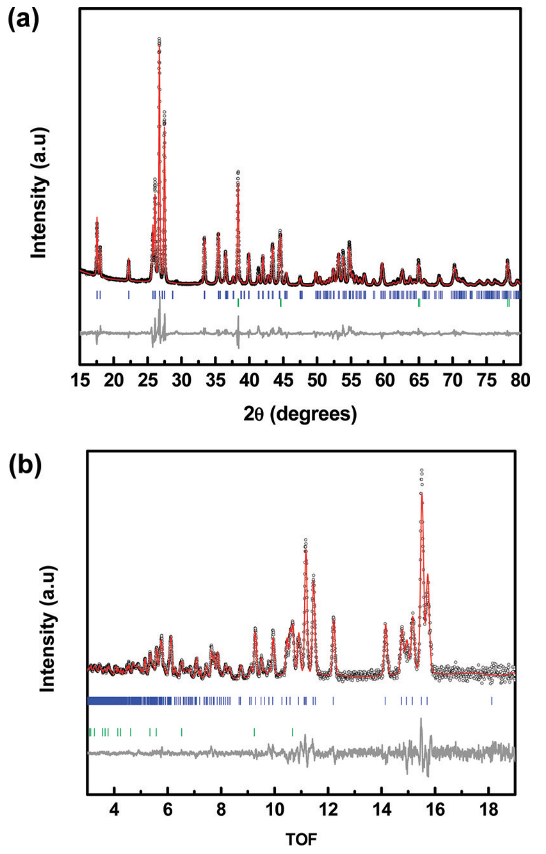

Figure 5. (a) X-ray diffraction pattern and (b) neutron diffraction pattern and Rietveld refinement of Li_2VPO_4F synthesized by chemical reduction of $LiVPO_4F$ with $LiAlH_4$. For each pattern, the experimental points are black, the fit is shown in red, the calculated reflections of Li_2VPO_4F are shown in blue, calculated reflections of Al are shown in green and the difference map is shown in gray. The lattice parameters and atomic positions are listed in Table 3.

$LiVPO_4F$ until almost complete intercalation of one equivalent of Li, where the reduced phase is the only vanadium fluorophosphate phase present. This phase has the stoichiometry Li_2VPO_4F, which was verified by elemental analysis that confirmed a Li:V:P ratio of very close to 2:1:1.

Table 3. Lattice Constants and Atomic Parameters for Li_2VPO_4F Refined from Combined X-ray and Neutron Diffraction Powder Data[a]

Li_2VPO_4F

space group: $C2/c$ (No. 15), monoclinic
M_w = 178.79 g/mol
D = 3.171 g cm^{-3}
a = 7.2255(1) Å
b = 7.9450(1) Å
c = 7.3075(1) Å
β = 116.771(1)°
V = 374.537(1) Å^3

atom	Wychoff	x/a	y/b	z/c	Occ.	U_{iso}
V(1)	4*b*	0	1/2	0	1.0	0.0058(1)
P(1)	4*e*	1/2	0.3563(1)	0.25	1.0	0.0068(1)
O(1)	8*f*	0.3266(2)	0.4700(1)	0.1069(2)	1.0	0.0095(1)
O(2)	8*f*	0.0813(3)	0.7447(1)	0.1266(2)	1.0	0.0095(1)
F(1)	4*e*	0	0.3640(1)	0.25	1.0	0.0088(1)
Li(1)	8*f*	0.1174(2)	0.1613(1)	0.1597(2)	0.5	0.014(1)
Li(2)	8*f*	0.1791(2)	0.2177(1)	0.4394(2)	0.5	0.014(1)

[a] X-ray diffraction agreement factors: R_{wp} = 11.08%, R_p = 8.40%, $R_F{}^2$ = 6.79%. Neutron diffraction agreement factors: R_{wp} = 4.28%, R_p = 7.93%, $R_F{}^2$ = 4.92% Combined statistics: R_{wp} = 9.24%, R_p = 8.40%.

Li_2VPO_4F was prepared ex-situ by stirring $LiVPO_4F$ with the chemical reducing agent $LiAlH_4$ in an inert atmosphere. Its X-ray diffraction and neutron diffraction patterns are shown in panels a and b in Figure 5, respectively, along with the combined Rietveld refinement. The fits and resultant lattice parameters/atomic positions are listed in Table 3. A comparison of the structures of $LiVPO_4F$ and Li_2VPO_4F (Figure 6) makes it clear that although Li_2VPO_4F ($C2/c$) crystallizes in a different space group than $LiVPO_4F$ ($P\bar{1}$), Li_2VPO_4F is closely related to the parent phase. The exact same structural motif is present in Li_2VPO_4F, namely one-dimensional chains of VO_4F_2 octahedra which propagate (in the $C2/c$ cell) along the c-axis and that are connected by phosphate tetrahedra to form a fully corner-shared framework. Li ions partially occupy two general sites: Li1 ions reside in octahedral sites along the edges of the (110) tunnels (see Figure 6). These

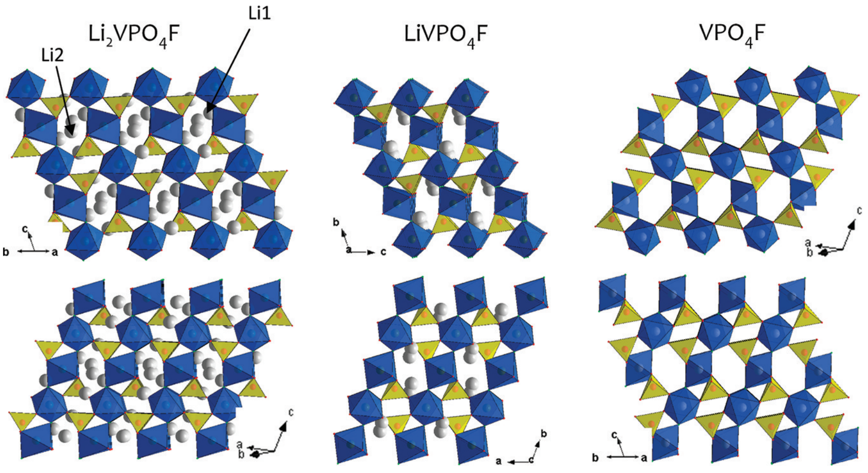

Figure 6. Pictorial representation of the structures of VPO_4F, $LiVPO_4F$, and Li_2VPO_4F depicting the chains of corner-shared vanadium octahedra and phosphate tetrahedra common to each structure. The vanadium octahedra are shown in blue, phosphate tetrahedra are shown in yellow, and the Li atoms are shown in white.

Table 4. Lattice Constants and Atomic Parameters of VPO_4F Refined from Powder XRD Data[a]

VPO_4F

Space group: C 2/c (#15), Monoclinic
M_w = 164.91 g/mol
D = 3.434 g cm^{-3}
a = 7.1553(2) Å
b = 7.1014(1) Å
c = 7.1160(2) Å
β = 118.089(1)°
V = 319.001(8) $Å^3$

atom	Wychoff	x/a	y/b	z/c	Occ.	U_{iso}
V	4*d*	0.25	−0.25	0	1.0	0.015(1)
P	4*e*	0.5	0.1245(3)	0.25	1.0	0.012(1)
F	4*e*	0	−0.1684(5)	−0.25	1.0	0.014(1)
O (1)	8*f*	0.3309(3)	0.0037(4)	0.0749(4)	1.0	0.012(1)
O (2)	8*f*	0.3951(3)	0.2479(4)	0.3456(2)	1.0	0.014(1)

[a] Agreement factors: R_{wp} = 8.88%, R_p = 6.80%, $R_F{}^2$ = 4.76%.

sites are nested between pairs of V octahedra and the Li1 site shares edges with both vanadium sites. This site is quite similar in location to the original split Li position in $LiVPO_4F$. Although the change in symmetry of the lattice in lithiation makes this difficult to determine from the fractional coordinates, visual comparison of the frameworks shows it clearly (Figure 6). The Li ions which reside in the Li2 sites are located at the center of the (110) tunnels and also sit between pairs of vanadium octahedra. The Li2 ions are face-shared with both vanadium octahedra of the pair, and correspond to the lithium that is inserted on reduction (ie, the new site). The structure of Li_2VPO_4F differs considerably from other Li_2MPO_4F compounds such as Li_2FePO_4F[15] and Li_2NiPO_4F,[41] both of which crystallize in orthorhombic space groups, *Pbcn* and *Pnma*, respectively.

The volume change for the transition from $LiVPO_4F$ to Li_2VPO_4F (7.4%) is fairly typical for phosphates, and the lattice mismatch between the two phases is one of the main reasons the electrochemical potential is flat in this region.

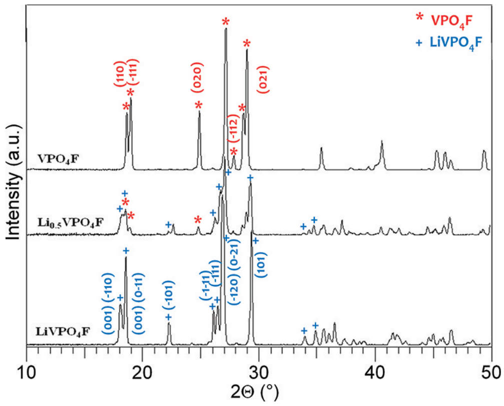

Figure 7. X-ray powder diffraction patterns of $Li_{1-x}VPO_4F$, synthesized by the chemical oxidation of $LiVPO_4F$ with $NOBF_4$. Two-phase behavior was observed up to the formation of VPO_4F.

Figure 7 shows the evolution in the XRD patterns of $Li_{1-x}VPO_4F$ from x = 0 to x = 1 formed upon chemical oxidation of $LiVPO_4F$ with $NOBF_4$ under an argon atmosphere. On partial oxidation of $LiVPO_4F$ to $Li_{0.5}VPO_4F$, a mixture of $LiVPO_4F$ and a new phase is apparent in the diffraction pattern. Complete oxidation shows only the presence of this new phase, namely VPO_4F. An X-ray diffraction pattern and subsequent Rietveld refinement on the pure VPO_4F powder sample is shown in Figure 8 and the refinement results are summarized in Table 4. The structure (Figure 6) is also strongly related to $LiVPO_4F$, and is also isostructural with $FeSO_4F$ which crystallizes in the same *C*2/*c* lattice.[42] VPO_4F consists of corner-shared chains of VO_4F_2 octahedra interconnected by phosphate groups via corner-sharing where the tunnels are obviously free of lithium ions. The volume change for the transition from $LiVPO_4F$ ↔ VPO_4F is 8.5%, roughly 2% greater than the volume difference for $LiFePO_4$ → $FePO_4$, which is one of the reasons two-phase behavior is observed in this region of the electrochemical curve. This is substantially larger than in $LiFePO_4$ ↔ $FePO_4$ olivine, for example (6.7%), and yet the two phase electrochemical transition takes place with very low polarization suggestive of high Li-ion mobility and relatively rapid kinetics.

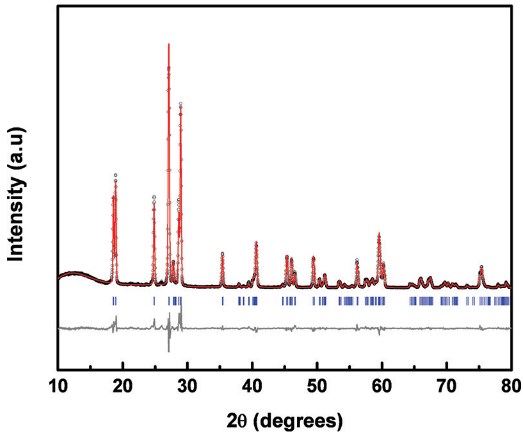

Figure 8. X-ray diffraction pattern and Rietveld refinement of VPO_4F synthesized by chemical oxidation of $LiVPO_4F$. The experimental points are black, the fit is shown in red, the calculated reflections are shown in blue, and the difference map is shown in gray. The lattice parameters and atomic positions are listed in Table 4.

Solid-State NMR. The "split" crystallographic site for lithium in $LiVPO_4F$ was observed as a broad line in the ^7Li

MAS NMR spectrum collected at 330 K (MAS = 40 kHz), with a paramagnetic shift centered at an average of 112 ppm (Figure 9). This broad line could be deconvoluted into two resonances separated by 3 ppm with a ratio very similar to the Rietveld refinement of the split site using a "blind fit", although other constrained fits also provided a reasonable fit. The chemical shift range for ^{6}Li and ^{7}Li is normally on the order of ±10 ppm. The high value for the observed shift is attributed to the geometry dependent hyperfine coupling of the Li-nuclei with the unpaired electron density sitting on the V^{3+} transition metal center.[43] The relatively short spin−lattice relaxation time (T_1) of this resonance (6.5 ± 0.2 ms) also reflects the paramagnetic nature of the Li-resonance. The high frequency shift of 112 ppm is consistent with that reported for other lithium vanadium(III) phosphates.[44,45]

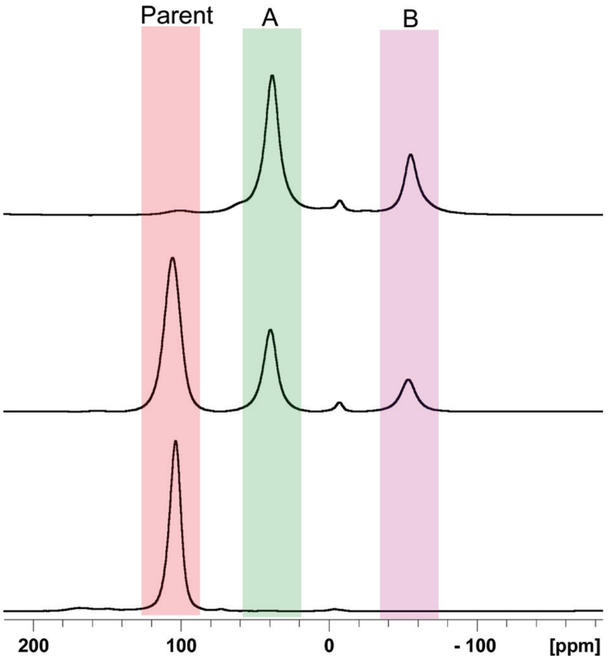

Figure 9. ^{7}Li MAS (40 kHz, 330 K) spectra of $LiVPO_4F$ at various stages of lithiation.

Upon 50% lithiation of $LiVPO_4F$ to form $Li_{1.5}VPO_4F$, two new resonances emerge. The first is centered at 46 ppm and the second at −47 ppm, measured under 40kHz MAS (at 330 K). These sites are herein referred to as sites A and B, respectively. The peak belonging to the parent $LiVPO_4F$ phase remains but broadens slightly. A resonance centered at 0 ppm is also observed and is attributed to a diamagnetic Li impurity as it has a considerably longer T_1 relaxation time (>60 s). After lithiation to Li_2VPO_4F, a slight amount of the parent $LiVPO_4F$ remains but resonances belonging to the A and B sites now dominate the spectrum. Integration of these sites over the entire sideband manifold yields a ratio of 1:1 for the A:B sites, which clearly correspond to the two independent lithium ions in the fully reduced phase. The ^{7}Li spin−lattice relaxation times for sites A and B are 3.2 ± 0.2 and 2.0 ± 0.2 ms, respectively. The lower times vis-à-vis the parent $LiVPO_4F$ are consistent with the increase in unpaired electron spin density observed in these systems that leads to stronger electron-Li dipolar coupling values. As we will prove in the following discussion, the resonance A at 46 ppm closely corresponds to the position of the original split Li site in $LiVPO_4F$ (at 112 ppm) which is assigned to Li1 in Li_2VPO_4F (see Figure 6). The shift of ~65 ppm to lower frequency is in good accord with that observed for a 1 e^- Fermi contact shift exhibited on reducing the V^{IV} to V^{III} in other similar compounds. An example is the redox couple in $Li_1V_2(PO_4)_3 \leftrightarrow Li_2V_2(PO_4)_3$, where the addition of one d-electron in a t_{2g} orbital was found to contribute a lower frequency shift of 77 ppm. The new site (resonance B at −47 ppm) that corresponds to Li2 in Li_2VPO_4F experiences a much more significant low frequency chemical shift, which is discussed below.

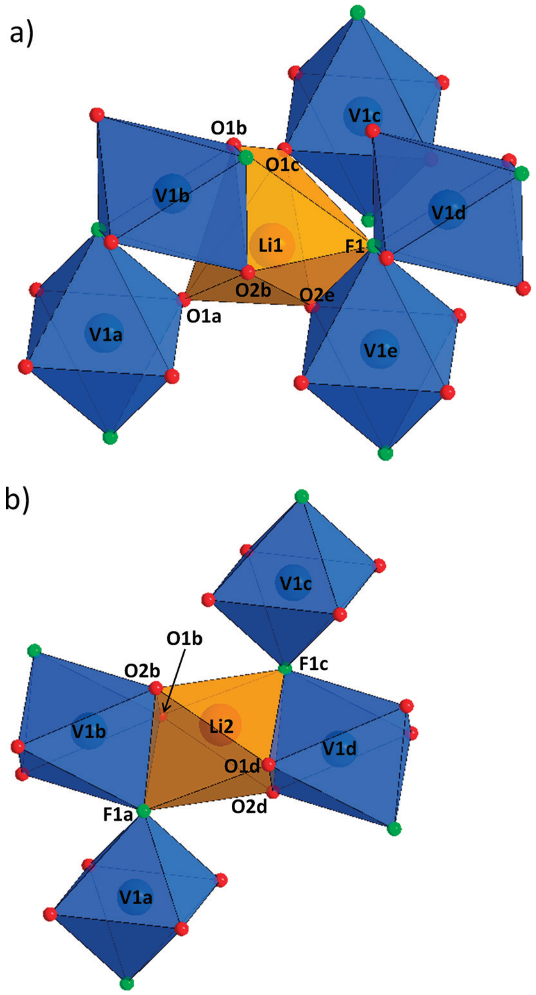

Figure 10. Pictorial representation of (a) the Li1 site and (b) the Li2 site in Li_2VPO_4F. The Li sites are shown in orange and the surrounding vanadium octahedra in blue. Phosphate groups omitted for clarity.

To answer the question of which Li sites in the Li_2VPO_4F structure (whose local environments are shown in Figure 10) correlate to the A and B resonances, we analyzed the geometry dependent hyperfine coupling between the unpaired electron spin density and the Li atoms.[44,46] There are two mechanisms for electron spin density transfer which are found to be most effective when the Li−O−V (or Li−F−V) orbitals overlap at angles close to 90 or 180°. Because Li_2VPO_4F has orbital overlap angles closer to 90°, the 180° interactions are ignored. For the mechanisms involving 90° orbital overlap, unpaired electron spin density sitting in the t_{2g} orbital of V in an

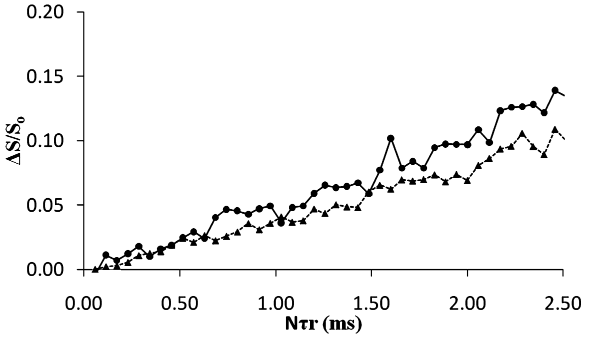

Figure 11. ^{6}Li{^{19}F} REDOR buildup curves for resonances A (triangles) and B (circles). MAS = 35 kHz.

octahedral environment is able to delocalize onto the Li s orbital leading to an increase in the paramagnetic shift. Comparison of the local Li environments of Li1 and Li2 in reference to the V centers clearly shows that Li1 has a larger number of Li—O—V angles closer to 90° than does Li2 (Figure 10). A greater amount of electron density spin density is therefore localized on the Li nucleus meaning a higher paramagnetic shift is observed. As well, Li1 resides in the analogous structural position to the split Li site in the parent material, $LiVPO_4F$, and is changed by roughly 70 ppm, as expected for the change in oxidation state at the vanadium center (vida supra). Therefore, resonance A is assigned to Li1. Conversely, Li2 has much poorer Li—O—V and Li—F—V overlap and gives rise to the lower frequency resonance labeled B. It is interesting to note that, while the two sites can be distinguished from each other and assigned based on these arguments, there is not an obvious justification for the significantly negative chemical shift observed for Li2. Related studies of the transition metal olivines have shown similarly negative chemical shifts for the Ni and Co phases, which were correlated with the number of unpaired electrons, and which orbital they occupy.[47] Another factor may be that Li2 is face-shared between two vanadium sites (Figure 10), whereas Li1 is edge-shared between two vanadium sites, but as both sites have 4 Li—O—V interactions close to 90 degrees the impact of this is not clear.

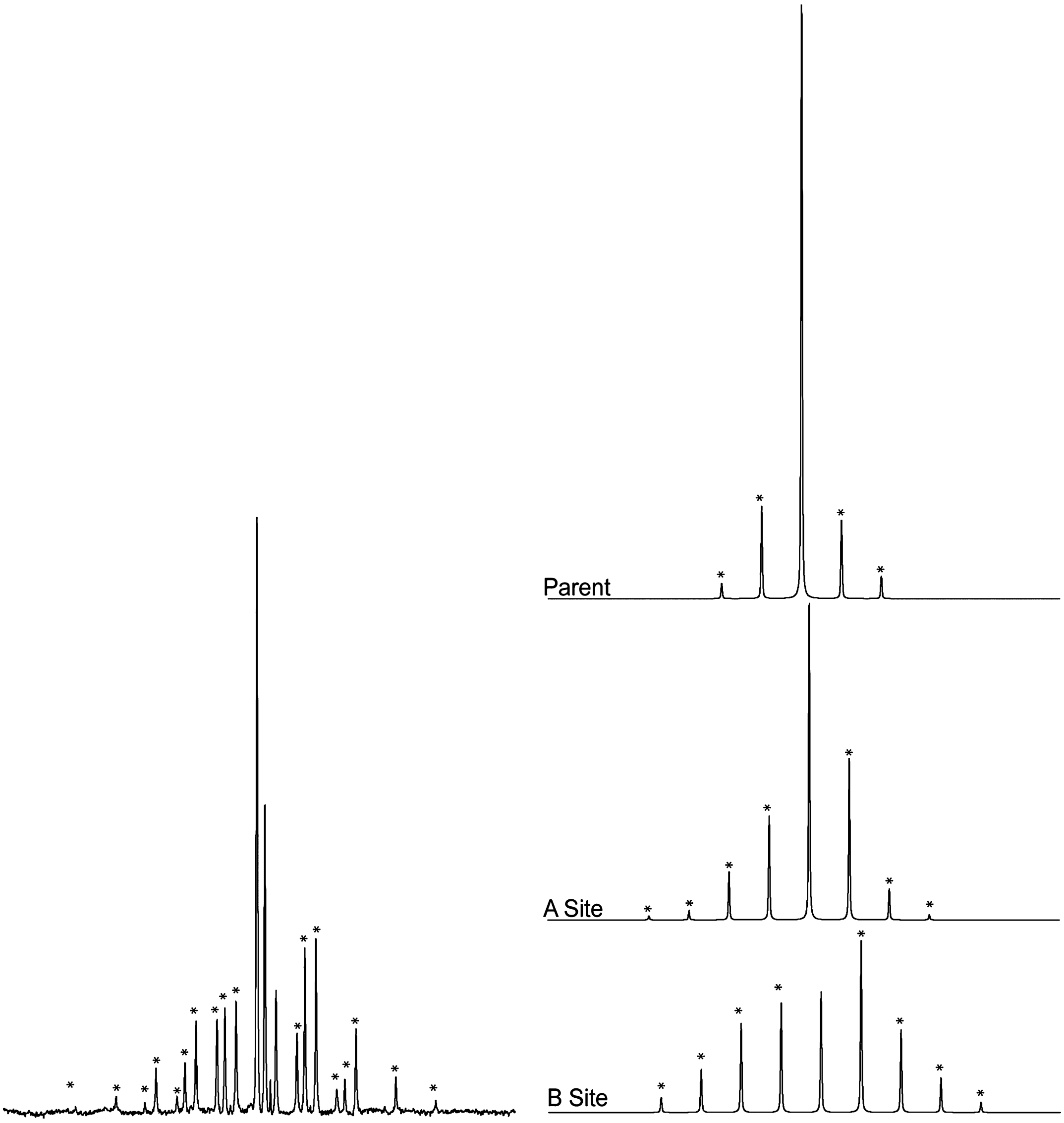

Figure 12. Deconvolution of sideband manifold for ^{7}Li MAS spectrum of $Li_{1.5}VPO_4F$. Experimental spectrum shown on left. Sideband manifold belonging to each of the crystallographic Li sites (as modeled in DMfit) on right. From top to bottom on right-hand side – modeled manifold for parent $LiVPO_4F$, A site, and B site. Asterisks denote spinning sidebands.

Table 5. Summary of ^{7}Li Spin−Lattice Relaxation Times (T_1) for $LiVPO_4F$ and Li_2VPO_4F

	T_1 times (ms)		
sample	parent $LiVPO_4F$	A	B
$LiVPO_4F$	6.5 ± 0.2		
Li_2VPO_4F		3.2 ± 0.2	2.0 ± 0.2

Table 6. Summary of ^{6}Li Spin−lattice Relaxation Times (T_1) for $Li_{1.5}VPO_4F$ and Li_2VPO_4

	T_1 times (ms)		
sample	parent $LiVPO_4F$	A	B
$Li_{1.5}VPO_4F$	44.2 ± 0.5	22.9 ± 0.5	16.8 ± 0.5
Li_2VPO_4F		22.7 ± 0.5	16.3 ± 0.5

This assignment was further confirmed by correlating each of the Li sites to the single F environment using ^{6}Li−^{19}F rotational echo, double resonance (REDOR) measurements. ^{6}Li{^{19}F}REDOR reintroduces ^{6}Li−^{19}F dipolar couplings that are averaged through MAS. The observed nucleus (^{6}Li) is measured using a spin−echo sequence with (S) and without (S_0) the application of a series of π pulses on the dephased nucleus (^{19}F). The normalized difference in ^{6}Li signal intensity ($[S_0 - S]/S_0$) is then plotted as a function of the dipolar evolution time ($N\tau_R$ = number of rotor periods times the rotor period). Stronger REDOR buildup curves arise from stronger dipolar couplings (D_{ij}) which are inversely dependent on the internuclear distance between the two spins (i and j) (eq 1),

$$D_{ij} = \mu_0\left(\frac{\hbar}{4\pi}\right)\frac{1}{r^3}\gamma_i\gamma_j \qquad (1)$$

where γ_i and γ_j are the gyromagnetic ratios of the two spins. Figure 11 shows the ^{6}Li{^{19}F} REDOR curves observed for resonances A and B. The stronger REDOR buildup for the B resonance (Li2) is consistent with this site having one short Li−F internuclear distance of 1.82 Å, and a second Li−F contact at 2.49 Å (see Table 7) . The single Li1−F distance of 2.06 Å gives rise to the weaker REDOR buildup curve for resonance A (Li1).

Separation of the sideband manifolds belonging to the different Li sites allows for a more detailed analysis of the Li-environments within this system. A ^{7}Li MAS spectrum showing the full sideband manifold of $Li_{1.5}VPO_4F$ is shown in Figure 12. Using the DMFit program, the sideband manifolds of each Li site were modeled.[48] This allowed for determination of the chemical shift anisotropy (Δ_{cs}), axial symmetry (η), and span (Ω) of each site (Table 8). The substantial increase in the span of the sideband manifolds of A and B (Ω = 2400 and 2700 ppm, respectively) as compared to the parent $LiVPO_4F$ (Ω = 1350 ppm) is consistent with the increase in electron spin density sitting on the transition metal center. This increase leads to stronger electron-Li dipolar coupling interaction which largely governs the span of CSA in paramagnetic systems.[3] When comparing the Li1 and Li2 sites, the larger anisotropy of the Li2 site vs the Li1 site (Δ_{cs} = 1205 ppm vs 705 ppm) is expected as Li1 is a six coordinate site (LiO_5F), whereas the Li2 sits in a much more asymmetric environment composed of a five coordinate LiO_3F_2 polyhedra with an additional long Li−O bond (see Figure 10 and Table 7).

Table 7. Summary of Li1−X−V and Li2−X−V Bond Angles for the Li1 and Li2 Environments, Respectively, in Li_2VPO_4F[a]

Li1−X−V	Li1−X−V angle (deg)	Li−V distance (Å)
Li1−O1a−V1a	108.30	3.681
Li1−O1b−V1b	89.61	3.046
Li1−O2b−V1b	91.45	3.046
Li1−O1c−V1c	135.00	4.268
Li1−F1−V1d	146.35	4.006
Li1−F1−V1e	87.86	2.904
Li1−O2e−V1e	87.72	2.904
Li2−X−V	Li2−X−V angle (deg)	Li−V distance (Å)
Li2−F1a−V1a	123.77	4.074
Li2−F1a−V1b	73.10	2.764
Li2−O1b−V1b	83.86	2.764
Li2−O2b−V1b	84.05	2.764
Li2−F1c−V1c	134.62	3.643
Li2−F1c−V1d	86.92	2.724
Li2−O1d−V1d	66.15	2.724
Li2−O2d−V1d	86.99	2.724

[a] Refer to Figure 10 for atomic designations.

Table 8. Summary of CSA Parameters for Individual Sites of $Li_{1.5}VPO_4F$

Li site	Ω (ppm)	Δ_{cs} (ppm)	η
parent $LiVPO_4F$	1350	435	0.8
A	2400	736	0.5
B	2700	1206	0.75

We explored exchange of the Li$^+$ between these two sites using 2D EXSY experiments. In these studies, each spin is frequency labeled during the evolution period, t_1. The exchange processes are allowed to take place during a mixing period of set length, τ_m, which is limited by the T_1 times of the nuclei. Cross peaks appear at off-diagonal sites corresponding to the sites involved in the exchange process. Samples partially enriched with ^{6}Li (which has an inherently longer T_1, see Tables 5 and 6) were used for the exchange experiments in order to probe mixing times long enough for exchange processes to occur. Spin−lattice relaxation times of both spins were determined at room temperature for ^{6}Li using a nonselective inversion recovery experiment, and found to be 22.7 ± 0.5 and 16.3 ± 0.5 ms for sites A and B, respectively (Table 6). Figure 13a shows ^{6}Li 2D EXSY spectra acquired at 303 K for $Li_{1.5}VPO_4F$. Although no Li-exchange between the crystallographic sites takes place at this temperature, crosspeaks between the A and B sites are observed are clearly evident following an increase in temperature to 330 K (Figure 13b). The mixing time in these experiments was extended to 15 ms, which provided sufficient time for the exchange process to take place. Evaluation of the activation energy of this exchange process could not be determined using the 2D version of the exchange spectroscopy, because the relatively slow correlation time does not fall within the limits of spin−lattice relaxation times of both spins. To overcome this limitation, the 1D version of the EXSY experiment, together with chemical exchange calculations which include both relaxation and ion dynamics contributions to the exchange matrix have been utilized. Using this methodology, the activation energy for ion exchange between sites A and B was determined to be 0.45 eV,

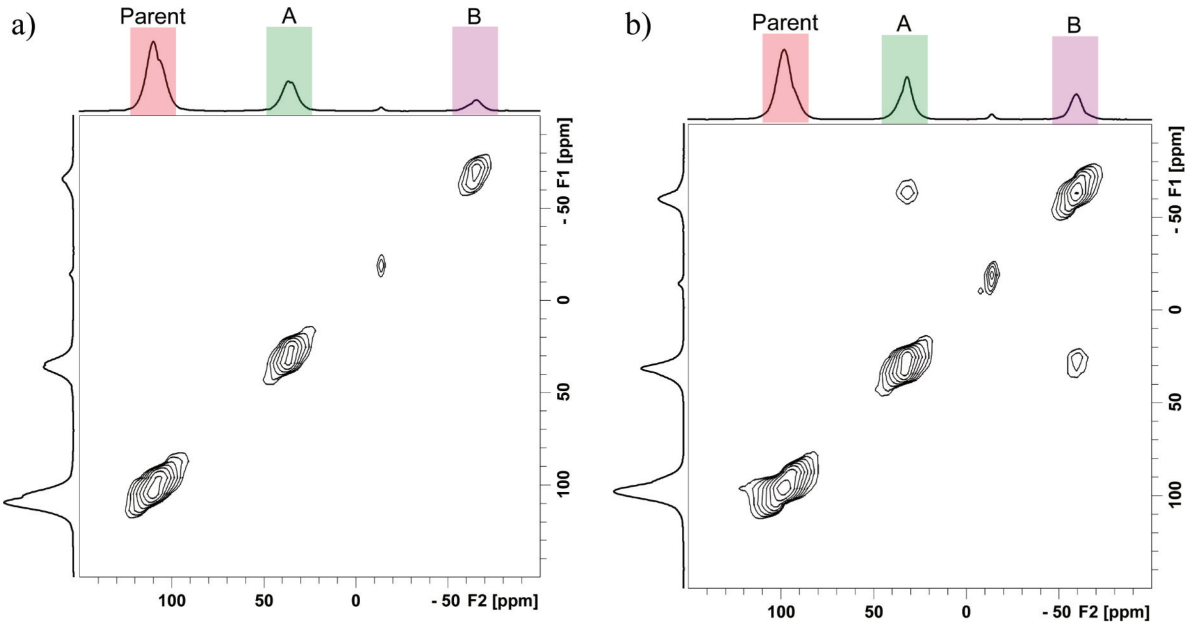

Figure 13. ^{6}Li 2D EXSY spectrum over a variable temperature range shows evidence of thermally activated chemical exchange in the Li_2VPO_4F phase. (a) T = 303 K (MAS = 25 kHz) and (b) T = 330 K (MAS = 40 kHz). For both experiments, τ_{mix} = 15 ms.

as will be reported in a subsequent publication. We note that similar low activation energies for Li ion hops of 0.4 eV in the fluorosulphate tavorite, $LiFeSO_4F$, have been calculated using atomistic modeling methods.[49]

■ CONCLUSIONS

We determined the structural relationship between the three members of the two-electron redox couple that spans the tavorite-type series of fluorophosphates $Li_{1\pm x}VPO_4F$ (x = 0,1) using a combination of X-ray and neutron diffraction, and report for the first time the isolation and structure of the two extreme end members, VPO_4F and Li_2VPO_4F. The three materials have closely related structures that result in two-phase transitions either on oxidation or reduction of 1e$^-$ (and Li$^+$) from $LiVPO_4F$. A slight change in symmetry accompanies this process, and the parent structure converts from $P\bar{1}$ to $C2/c$ in both cases owing to a small "twist" in the framework. Overall, the two electron redox couple spans a substantial volume change of 15.9%, which might be expected to give large electrochemical polarization because of the difficulty of phase boundary transport. However, the polarization at intermediate rates is very low, which is likely due to facile ion transport in the tavorite-type lattice. Solid-state ^{6,7}Li NMR studies of Li_2VPO_4F allow us to distinguish the two lithium sites that exchange at slightly above room temperature (330 K), with a low activation energy in accord with our previous modeling studies.

■ AUTHOR INFORMATION

Corresponding Author

*E-mail: lfnazar@uwaterloo.ca.

■ ACKNOWLEDGMENTS

We are deeply appreciative to Dr. Marnix Wagemaker (TU Delft) for acquiring the neutron diffraction pattern at ISIS. Use of the Advanced Photon Source at Argonne National Laboratory was supported by the U.S. Department of Energy, Office of Science, Office of Basic Energy Sciences, under Contract DE-AC02-06CH11357. LFN and GRG acknowledge NSERC for funding through their Discovery and CRD (LFN) programs.

■ REFERENCES

(1) Pahdi, A. K.; Nanjundaswamy, K. S.; Goodenough, J. B *J. Electrochem. Soc.* **1997**, *144*, 1188.

(2) Pahdi, A. K.; Nanjundaswamy, K. S.; Masquelier, C.; Okada, S.; Goodenough, J. B *J. Electrochem. Soc.* **1997**, *144*, 1609.

(3) Drezen, T.; Kwon, N.-H.; Bowen, P.; Teerlinck, I.; Isono, M.; Exnar, I *J. Power Sources* **2007**, *174*, 949.

(4) Wang, D.; Buqab, H.; Crouzet, M.; Deghenghi, G.; Drezen, T.; Exnar, I.; Kwon, N.-H.; Miners, J H.; Poletto, L.; Gratzel, M *J. Power Sources* **2009**, *189*, 624.

(5) Reale, P.; Scrosati, B.; Delacourt, C.; Wurm, C.; Morcrette, M.; Masquelier, C *Chem. Mater.* **2003**, *15*, 5051.

(6) Whittingham, M. S.; Song, Y.; Lutta, S.; Zavalij, P. Y.; Chernova, N. A *J. Mater. Chem.* **2005**, *15*, 3362.

(7) Chung, S.-Y.; Bloking, J. T.; Chiang, Y-M *Nat. Mater.* **2002**, *1*, 123.

(8) Ellis, B.; Herle, P. S.; Rho, Y. H.; Nazar, L. F.; Dunlap, R.; Perry, L. K.; Ryan, D. H *Faraday Discuss.* **2007**, *134*, 119.

(9) Li, J.; Yao, W.; Martin, S.; Vaknin., D *Sol. Stat. Ion.* **2008**, *179*, 2016.

(10) Kim, D. H.; Im, J. S.; Kang, J. W.; Kim, E. J.; Ahn, H. Y.; Kim, J. *J. Nanosci. Nanotechnol.* **2007**, *7*, 3949.

(11) Sides, C. R.; Croce, F.; Young, V. Y.; Martin, C. R.; Scrosati, B *Electrochem. Solid-State Lett.* **2005**, *8*, A484.

(12) Gaberscek, M.; Dominko, R.; Jamnik, J *Electrochem. Commun.* **2007**, *9*, 2778.

(13) Huang, H.; Yin, S. C.; Nazar, L. F *Electrochem. Solid-State Lett.* **2001**, *4*, A170.

(14) Kang, B; Ceder, G. *Nature* **2009**, *458*, 190.

(15) Ellis, B.; Makahnouk, W. R. M.; Makimura, Y.; Toghill, K.; Nazar, L. F *Nat. Mat.* **2007**, *6*, 749.

(16) Ellis, B. L.; Makahnouk, W. R. M; Rowan-Weetaluktuk, W. N.; Ryan, D. H.; Nazar, L. F *Chem. Mater.* **2010**, *22*, 1059.

(17) Yakubovich, O. V.; Urusov, V. S *Geokhimiya* **1997**, *7*, 720.

(18) Groat, L. A.; Raudsepp, M.; Hawthorne, F. C.; Ecrit, T. S.; Sherriff, B. L.; Hartman, J. S *Am. Mineral.* **1990**, *75*, 992.

(19) Aranda, M. A. G.; Attfield, J. P.; Bruque, S *Angew. Chem., Int. Ed.* **1992**, *31*, 1090.
(20) Beitone, L.; Guillou, N.; Millange, F.; Loiseau, T.; Ferey, G *Solid State Sci.* **2002**, *4*, 1061.
(21) Sebastian, L.; Gopalakrishnan, J.; Piffard, Y *J. Mater. Chem.* **2002**, *12*, 374.
(22) Recham, N.; Chotard, J.-N.; Dupont, L.; Delacourt, C.; Walker, W.; Armand, M.; Tarascon, J-M *Nat. Mater.* **2010**, *9*, 68.
(23) Tripathi, R.; Ramesh, T. N.; Ellis, B. L.; Nazar, L. F *Angew. Chem.* **2010**, *49* (46), 8738.
(24) Ramesh, T. N.; Lee, K. T.; Ellis, B. L.; Nazar, L. F *Electrochem. Solid-State Lett.* **2010**, *13*, A43.
(25) Recham, N.; Chotard, J.-N.; Jumas, J.-C.; Laffont, L.; Armand, M.; Tarascon, J-M *Chem. Mater.* **2010**, *22*, 1142.
(26) Barker, J.; Saidi, M. Y.; Swoyer, J. L *J. Electrochem. Soc.* **2003**, *150*, A1394.
(27) Barker, J.; Gover, R. K. B.; Burns, P.; Bryan, A.; Saidi, M. Y.; Swoyer, J. L *J. Power Sources* **2005**, *146*, 516.
(28) Barker, J.; Saidi, M. Y.; Swoyer, J. L U.S. Patent 6 855 462 B2, 2005.
(29) Barker, J.; Gover, R. K. B.; Burns, P.; Bryan, A *Electrochem. Solid-State Lett.* **2005**, *8*, A285.
(30) Wang, J.; Toby, B. H.; Lee, P. L.; Ribaud, L.; Antao, S. M.; Kurtz, C.; Ramanathan, M.; Von Dreele, R. B.; Beno, M. A *Rev. Sci. Instrum.* **2008**, *79*, 085105−1.
(31) Lee, P. L.; Shu, D.; Ramanathan, M.; Preissner, C.; Wang, J.; Beno, M. A.; Von Dreele, R. B.; Ribaud, L.; Kurtz, C.; Antao, S. M.; Jiao, X.; Toby, B. H *J. Synchrotron Radiat.* **2008**, *15*, 427.
(32) Preissner, C.; Shu, D.; Toby, B. H.; Lee, P.; Wang, J.; Kline, D.; Goetze, K. *Nucl. Instrum. Meth. Phys. Res., Sect. A* **2011**, in press.
(33) Dalesio, L. R.; Hill, J. O.; Kraimer, M.; Lewis, S.; Murray, D.; Hunt, S.; Watson, W.; Clausen, M.; Dalesio, J *Nucl. Instrum. Meth. Phys. Res., Sect. A* **1994**, *352*, 179.
(34) Larson, A. C.; Von Dreele, R. B *GSAS, General Structure Analysis System*; Los Alamos National Laboratory Report LAUR 86-748 ; os Alamos National Laboratory: Los Alamos, NM, 2000.
(35) Toby, B. H *J. Appl. Crystallogr.* **2001**, *34*, 210.
(36) Malcherek, T *Acta Crystallogr., Sect. B* **2002**, *58*, 607.
(37) Marion, D.; Ikura, M.; Tschudin, R.; Bax, A. *J. Magn. Reson.* **1989**, *85*, 393.
(38) Grey, C. P.; Cheetham, A. K.; Dobson, C. M. *J. Magn. Reson., Ser. A* **1993**, *101*, 299.
(39) Groat, L. A.; Chakoumakos, B. C.; Brouwer, D. H.; Hoffman, C. M.; Fyfe, C. A.; Morell, H.; Schultz, A. J *Am. Mineral.* **2003**, *88*, 195.
(40) Marx, N.; Croguennec, L.; Carlier, D.; Wattiaux, A.; Le Cras, F.; Suard, E.; Delmas, C *Dalton Trans.* **2010**, *39*, 5108.
(41) Dutreilh, M.; Chevalier, C.; El-Ghozzi, M.; Avignant, D.; Montel, J. M *J. Solid State Chem.* **1999**, *142*, 1.
(42) Tripathi, R.; Ramesh, T. N.; Ellis, B.; Nazar, L. F. *Angew. Chem., Int. Ed.* **2010**, *49*, 8738.
(43) Grey, C. P.; Dupre, N. *Chem. Rev.* **2004**, *104*, 4493.
(44) Yin, S. C.; Grondey, H.; Strobel, P.; Anne, M.; Nazar, L. F. *J. Am. Chem. Soc.* **2003**, *125*, 10402.
(45) Cahill, L. S.; Chapman, R. P.; Britten, J. F.; Goward, G. R *J. Phys. Chem. B* **2006**, *110*, 7171.
(46) Carlier, D.; Menetrier, M.; Grey, C. P.; Delmas, C.; Ceder, G *Phys. Rev.* **2003**, *67*, 174103.
(47) Tucker, M. C.; Reimer, J *J. Am. Chem. Soc.* **2002**, *124*, 3832.
(48) Massiot, D.; Fayon, F.; Capron, M.; King, I.; Le Calve, S.; Alonso, B.; Durand, J. O.; Bujoli, B.; Gan, Z. H.; Hoatson, G. *Magn. Reson. Chem.* **2002**, *40*, 70.
(49) Tripathi, R.; Gardiner, G.; Islam, M. S.; Nazar, L. F. *Chem. Mater.* **2011**, *23*, 2278.